Electron-phonon coupling in a system with broken symmetry: Surface of Be(0001)

TeYu Chien (簡德宇),[1,*] Xiaobo He,[2] Sung-Kwan Mo,[3] Makoto Hashimoto,[4] Zahid Hussain,[3] Zhi-Xun Shen,[5,6] and E. W. Plummer[2]

[1]*Department of Physics and Astronomy, University of Wyoming, Laramie, Wyoming 82071, USA*
[2]*Department of Physics and Astronomy, Louisiana State University, Baton Rouge, Louisiana 70803, USA*
[3]*Advanced Light Source, Lawrence Berkeley National Laboratory, Berkeley, California 94720, USA*
[4]*Stanford Synchrotron Radiation Lightsource, SLAC National Accelerator Laboratory, 2575 Sand Hill Road, Menlo Park, California 94025, USA*
[5]*Stanford Institute for Materials and Energy Sciences, SLAC National Accelerator Laboratory, 2575 Sand Hill Road, Menlo Park, California 94025, USA*
[6]*Geballe Laboratory for Advanced Materials, Departments of Physics and Applied Physics, Stanford University, Stanford, California 94305, USA*

(Received 18 April 2012; revised manuscript received 1 July 2015; published 21 August 2015)

The momentum-resolved Eliashberg function (ELF) $\alpha^2 F(\omega,\vec{k})$ for the Be(0001) zone-center surface state was extracted from the high-quality angle-resolved photoemission spectroscopy (ARPES) data at the Fermi energy in the $\bar{\Gamma} \rightarrow \bar{M}$ direction, displaying ten peaks. A comparison of the peaks in the ELF to the bulk phonon density of states (DOS) and the bulk and surface phonon dispersion allows for an identification of the origin of all but two of the peaks. The five high energy peaks (>52 meV) are associated with the coupling of the surface state to bulk phonon modes. The peaks at 44.5 and at 49.0 meV have contributions from both the bulk and surface phonons. The most intense peak at 37.5 meV is evidently having a contribution from electron-phonon coupling (EPC) of the surface state to the surface Rayleigh phonon mode. Surprisingly, the two lowest energy modes, which must be associated with surface Rayleigh phonon, cannot be attributed to a high phonon DOS at the surface nor to any Fermi surface nesting. After detail analysis, the three lowest energy peaks are associated with momentum dependence in the EPC matrix, reflected in the phonon linewidth changes. As a result of the broken symmetry at the surface, coupling of the initial surface state due to the presence of the surface phonons contributes ∼48.5 ± 12.5% of the spectral weight in the ELF and ∼66.5 ± 10.5% to the mass enhancement (λ).

DOI: 10.1103/PhysRevB.92.075133 PACS number(s): 73.20.−r, 71.38.−k, 79.60.Bm

I. INTRODUCTION

The interaction between electrons and various boson collective modes in a solid manifests itself in many physical observables, such as superconductivity [1–3], thermal conductance at interfaces [4], energy relaxation in nanoparticles [5], colossal magnetoresistance in ferromagnets [6], charge density wave formation in metals [7], and the Seebeck coefficients in nanoscale junctions [8]. Electron-phonon coupling (EPC), or electron-boson coupling in general, is becoming more important as the community investigates the functionality of complex materials such as electron correlated transition metal compounds, artificially structure thin films, and nanoparticles. This paper reports on the spectroscopic features in the EPC at the surface of a simple metal Be to clarify the nature of EPC in an environment of broken symmetry.

The EPC process couples an electron in an initial state $\vec{k}$ with an electron in a final state $\vec{k}'$, mediated by a phonon of energy ω and momentum $\vec{q}$. This process, which must conserve energy and momentum, renormalizes both the electronic band structure and the phonon dispersion. One of the significant advances in the last decade has been the development of angle-resolved photoemission spectroscopy (ARPES) as a means of measuring the EPC induced band renormalization near the Fermi energy. Very high quality APRES data has been used to perform an integral inversion of the real part of the self-energy determined experimentally to extract the Eliashberg function (ELF) [9,10]. In spite of unique capabilities of ARPES, these measurements only determine $\vec{k}$, leaving the identification of $\vec{k}'$ and $\omega(\vec{q})$ to theory. Here we attempt to identify the origin of the features in ELF by comparing the spectral features in the experimental ELF with the measured phonon density of states (DOS) and dispersion for both the surface and bulk. The assignments will be ensured by the satisfaction of the energy and the momentum conservations, namely $\varepsilon(\vec{k}') - \varepsilon(\vec{k}) = \omega(\vec{q})$ and $\vec{k}' - \vec{k} = \vec{q}$, respectively.

Physical properties at a surface or an interface are expected to be different from their bulk counterparts due to the broken translational symmetry, which can cause reconstruction and allows for spatially confined states (surface or interface states). The wave functions of the surface states are exponentially damped into the solid [11]. There are also localized surface phonon modes (Rayleigh waves) split off from the bottom of the bulk phonon bands [12,13]. The degree of localization of surface phonons or surface states will depend upon the nature of the mode—its energy and wave vector. For example, a zone center Rayleigh wave (RW) penetrates very deep into the bulk while the zone boundary RW can be localized at the surface [14]. The depth penetration of a surface state depends upon how far it is removed from the closest bulk band edge [11]. Moreover, it has been reported that the interplay between the surface electronic states and the bulk electronic states in the same region of the space (near the surface) could result in

*tchien@uwyo.edu

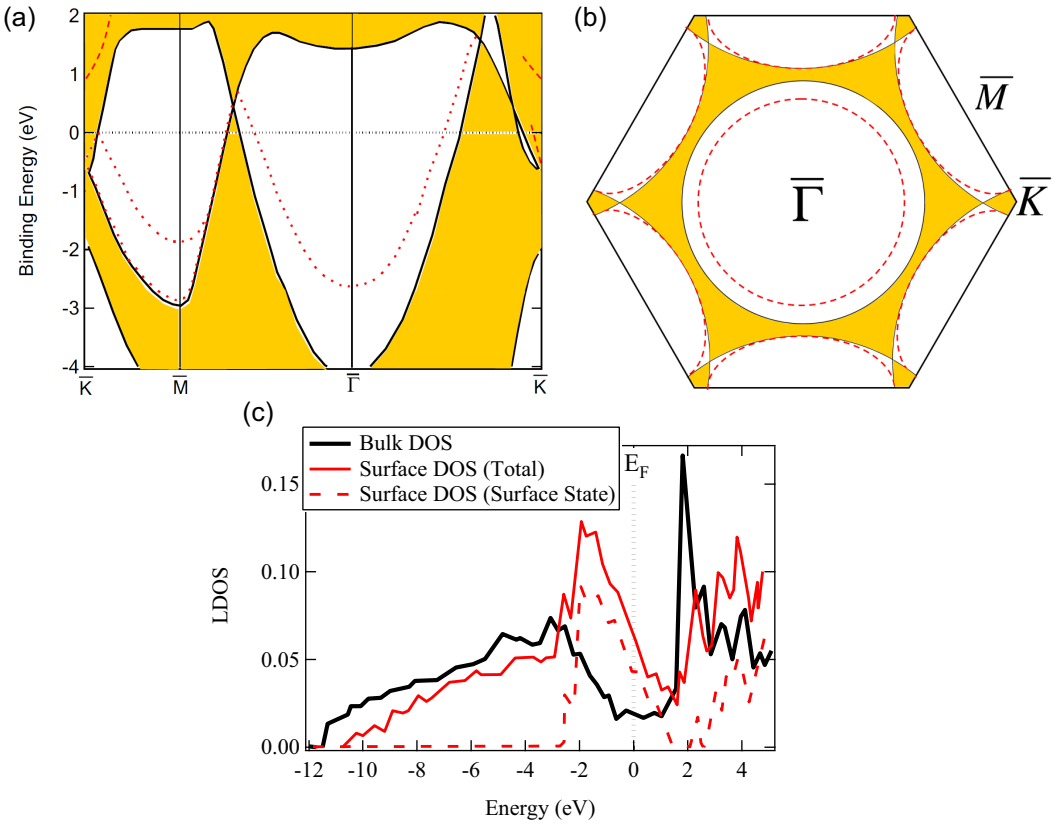

FIG. 1. (Color online) (a) Electronic band structures of Be(0001) surface [27]. Shadowed area represents the projection from bulk states; red dashed lines represent the surface states. (b) Fermi surface/contour of Be(0001) surface. Two surface states, $\bar{\Gamma}$ state (centered at $\bar{\Gamma}$) and $\bar{M}$ state (centered at $\bar{M}$), are shown with red dashed lines. (c) Electronic local density of states (LDOS) in Be bulk (black solid line) and at topmost Be(0001) layer (total: red solid line and surface state contribution: red dashed line) (from Ref. [11]).

acoustic surface plasmon due to charge oscillation between the two-dimensional (2D) and three-dimensional (3D) subsystems [15]. Therefore, at a surface, identifying the details of the EPC matrix element $|g[\vec{k},\vec{k}';\omega(\vec{q})]|^2$ can be complicated, since ARPES only determines $\vec{k}$, while $\vec{k}'$ and $\omega(\vec{q})$ can be either surface or bulk electronic and vibrational states, respectively. Even though a surface is a quasi-two-dimensional system, all of the integrals associated the EPC at a surface are three dimensional. For a truly 2D system the analysis is easier [16].

Beryllium is an ideal metal for the application of ARPES to study EPC. The top of the bulk phonon band is ∼80 meV, reducing the need for super high resolution. The bulk is almost a semimetal but the surface has well-defined and intense surface states, so that the surface DOS at the Fermi energy is ∼5 times that of the bulk [11]. A simple back of the envelope calculation indicates that this high density of states should result in an increased EPC with a mass enhancement λ of ∼1 compared to the bulk value of 0.24 [17]. In fact, Be(0001) was used in the first seminal papers describing APRES measurements of the band renormalization due to EPC, first by Jensen's group in 1998 [18] and then by the Baer's group in 1999 [19,20]. These early experiments have been followed by many other investigations with better signal to noise or a slightly different analysis procedure [9,18–23]. The reported mass enhancement λ for Be(0001) ranges from ∼0.6 [21,22] to ∼1 [18–20], which has been tabulated in a review [22]. Later, the inconsistency in experimental values of λ for Be(0001) was found to be the result of an anisotropic EPC [23]. However, the inconsistency between theory and experiment is still unresolved [23–25]. What motivated this study is to seek the origin of the inconsistency by identifying the origin and the contributions from each phonon mode experimentally.

The electronic properties of the Be(0001) surface are summarized in Fig. 1. The dispersion of the surface states on Be(0001) is shown in Fig. 1(a), with the surface Fermi contour displayed in Fig. 1(b). These states have been investigated both experimentally [19,20,26,27] and theoretically [28] for over 25 years. Both figures clearly show that there are two distinct surface states, the $\bar{\Gamma}$ state (centered at $\bar{\Gamma}$) and the $\bar{M}$ state (centered at $\bar{M}$). All of the previous measurements of EPC were made on the isotropic (in k space), nearly free-electron $\bar{\Gamma}$ state, which will be the focus in this paper as well. The presence of the surface states should alter the bulklike density of states near the surface. The surface is neutral so the charge to fill the surface states must come from bulklike states near the surface. Figure 1(c) shows the electronic local density of states (LDOS) in bulk Be and at the topmost Be(0001) surface. It is clear that the presence of the surface states (red dashed line) narrows the bandwidth at the surface and shifts the DOS up towards the Fermi energy, making the surface much more metallic than the bulk.

Before describing our measurements, let us discuss the difference between a surface and an inherently 2D material, like the layered perovskites, the dichalogenides, the cuprates, the Fe based superconductors, or graphene. If it is true that all the modes of the system (phonons or electrons) display very little dispersion in the direction perpendicular to the layers, then these systems can be treated as a real 2D system, simplifying the analysis of the data [16]. Undoubtedly there will be effects in the EPC resulting from the 3D nature of the material, but these should not be first order as they are in Be(0001), where the coupling of the surface state to the 3D bulk phonons contributes ~51.5% of the intensity in the ELF (will be discussed later). A general observation is that EPC in systems without broken symmetry, such as MgB_2, is well understood [29], but for systems with broken symmetry, such as substrate-supported graphene and Be(0001) surfaces, present theory is unsatisfactory [30,31]. It seems that the state-of-the-art theories fail to capture some essential ingredients of the EPC for systems with broken symmetry. Presumably, the broken symmetry at interfaces or artificially structured layers could make these systems equally complicated, i.e., a 3D problem with spatially dependent states.

As discussed earlier, the important quantity for EPC is the matrix element $g(\vec{k},\vec{k}';i)$, which couples electronic states $\vec{k}$ and $\vec{k}'$ through the phonon mode i [16,32]. The momentum resolved ELF $[\alpha^2F(\omega,\vec{k})]$ is given by [32]

$$\alpha^2F(\omega,\vec{k}) = \frac{V}{\hbar(2\pi)^3}\sum_i \int_{S_F} \frac{d^2\vec{k}'}{v_{\vec{k}'}} |g(\vec{k},\vec{k}';i)|^2 \delta[\omega - \omega(\vec{q};i)], \tag{1}$$

where $\vec{k}' = \vec{k} + \vec{q}$. The sum is over all phonon modes i (bulk and surface), with dispersion given by $\omega(\vec{q};i)$. The integral of $\vec{k}'$ is over the Fermi surface (both bulk and surface) S_F, with the electron velocity $v_{\vec{k}'}$, and contains the electron spectral weight of the initial state at $\vec{k}$. The EPC matrix element $g(\vec{k},\vec{k}';i)$ is given by [32]

$$g(\vec{k},\vec{k}';i) = -i\hat{\epsilon}(\vec{q};i)\cdot(\vec{k}-\vec{k}')\left[\frac{\hbar}{2MN\omega(\vec{q};i)}\right]^{1/2} V(\vec{k}-\vec{k}'), \tag{2}$$

where $\hat{\epsilon}(\vec{q};i)$ is the polarization vector (of unit length) of the phonon mode; $\omega(\vec{q};i)$ is the phonon dispersion relation; M and N are ion mass and total number of ions, respectively; and $V(\vec{k}-\vec{k}')$ is the effective potential experienced by an electron which interacts with the ion core and with all the other conduction electrons.

To illustrate the complexity associated with a surface, let us examine the ELF for a truly 2D system such as an isolated graphene layer, transition metal dichalcogenides, a cuprate [16], or any layered material with very small coupling between layers. The ELF is then written as

$$\alpha^2F(\omega,\vec{k}) = \frac{A}{\hbar(2\pi)^2}\sum_i \int_{C_F} \frac{d\vec{k}'}{v_{\vec{k}'}} |g(\vec{k},\vec{k}';i)|^2 \delta[\omega - \omega(\vec{q};i)], \tag{3}$$

where the integral of $\vec{k}'$ is over the Fermi contour (only surface states) in Eq. (3) and, in consequence, only the phonon modes with in-plane momentum will be needed. This contour integral in Eq. (3) is already much easier compared to Eq. (1) for a system of broken symmetry. When discussing quasi-two-dimensional systems with broken symmetry, like a surface, the sum and integral in Eq. (1) have to include all surface and bulk phonon modes and electronic states: it is a mixture between two-dimensional and three-dimensional systems and requires a 3D representation.

ARPES is an ideal method to study the EPC induced renormalization of the energy bands near the Fermi energy. The ELF can in principle be extracted from the experimentally determined electron self-energy $[\Sigma(\varepsilon,\vec{k},T) = \mathrm{Re}\Sigma(\varepsilon,\vec{k},T) + i\,\mathrm{Im}\Sigma(\varepsilon,\vec{k},T)]$ using the following definitions [9,32]:

$$\mathrm{Re}\Sigma(\varepsilon,\vec{k},T) = -\int_{-\infty}^{\infty} dv \int_0^{\omega_{\max}} d\omega' \alpha^2F(\omega',\vec{k}) \times \frac{2\omega'}{v^2-\varepsilon^2} f(v+\varepsilon,T), \tag{4}$$

$$\mathrm{Im}\Sigma(\varepsilon,\vec{k},T) = \pi\int_0^{\omega_{\max}} d\omega' \alpha^2F(\omega',\vec{k})[1 - f(\varepsilon-\omega',T) - 2n(\omega',T) + f(\varepsilon+\omega',T)], \tag{5}$$

where ε is the binding energy of the quasiparticle, T is the temperature of the system, $\omega_{\max}$ is the maximum phonon energy, and $f(\varepsilon,T)$ and $n(\varepsilon,T)$ represent the Fermi-Dirac and Bose-Einstein distribution functions, respectively. $\mathrm{Re}\Sigma(\varepsilon,\vec{k},T)$ renormalizes the electronic band structure near Fermi energy, creating the widely observed "kink" seen by ARPES [33]. $\mathrm{Im}\Sigma(\varepsilon,\vec{k},T)$ is related to the lifetime of quasiparticles, resulting in rapid increase in the spectrum width as a function of binding energy, saturating at the highest phonon energy [18–23,34–36]. The ELF has been extracted from the measured $\mathrm{Re}\Sigma(\varepsilon,\vec{k},T)$ using the maximum entrophy method (MEM) to do the integral inversion [9,10,34,37].

To illustrate the relationship between all of these functions we have created two different ELFs $[\alpha^2F(\omega)]$, based on the same phonon DOS, $F(\omega)$, but with a different coupling constant $\alpha^2(\omega)$, as shown in Fig. 2(a) [9,23]. For simplicity $F(\omega)$ and $\alpha^2(\omega)$ are assumed to be independent of the phonon momentum $\vec{q}$; and $\alpha^2(\omega)$ is a slowly varying function of the phonon energy ω. If there was Fermi surface nesting neither of these assumptions would be valid. Both ELFs are created to have the same mass enhancement factor, defined by $\lambda = 2\int_0^{\infty}\frac{\alpha^2F(\omega')}{\omega'}d\omega'$, as the measured value for Be(0001), $\lambda = 0.94$. The corresponding $\mathrm{Re}\Sigma(\varepsilon,\vec{k},T)$ and $\mathrm{Im}\Sigma(\varepsilon,\vec{k},T)$ calculated from Eqs. (4) and (5) are shown in Figs. 2(b) and 2(c), respectively. The measured dispersion relations can be obtained by combining the $\mathrm{Re}\Sigma(\varepsilon,\vec{k},T)$ with the bare-particle dispersion, and are shown in Fig. 2(d). The ARPES "kink," the signature of EPC or electron-boson coupling, can be seen in Fig. 2(d). An important message here is that even with the same λ, the low ELF in the low energy region could result in higher overall $\mathrm{Re}\Sigma(\varepsilon,\vec{k},T)$, which is very similar to the discrepancy between the state-of-the-art theoretical calculation and the experimental measurements (will be discussed later in Fig. 9). In this study, the reverse procedure was performed: APRES data is used to determine $\mathrm{Re}\Sigma(\varepsilon,\vec{k},T)$ by removing the bare

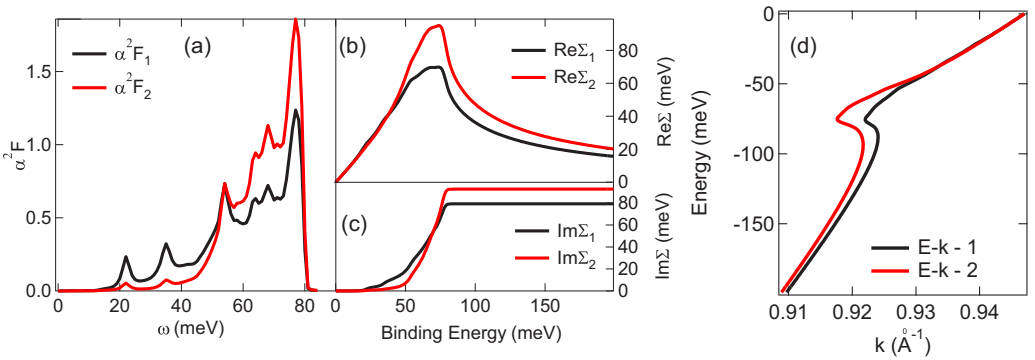

FIG. 2. (Color online) (a) Two different Eliashberg functions (ELF) $[\alpha^2F(\omega,\vec{k})]$. (b) and (c) The corresponding $\mathrm{Re}\Sigma(\varepsilon,\vec{k},T)$ and $\mathrm{Im}\Sigma(\varepsilon,\vec{k},T)$, respectively. Note that the two $\alpha^2F(\omega,\vec{k})$ are generated from the same phonon density of states but different electron-phonon coupling constants $[\alpha^2(\omega,\vec{k})]$, and have the same mass enhancement factors ($\lambda = 0.94$). (d) The two corresponding renormalized electron energy-momentum dispersion relations.

particle dispersion, and the ELF is extracted by using MEM for integral inversion of Eq. (4).

The rest of this paper is organized into three sections, Sec. II describes the experimental procedures, Sec. III presents the data and the process of extracting the ELF, and Sec. IV is a discussion of the origin of the spectral features in the extracted ELF. The later step will be accomplished by comparing the energy of the spectral features in the ELF with the measured and calculated phonon dispersions (bulk and surface). Finally, we will use this analysis to determine the location of $\vec{k}'$ (the final state) on the Fermi contours (surface and bulk). These results can be summarized as: (1) The high value of λ found for Be(0001) is primarily a result of the electrons in the surface state coupling to the low energy surface RW; and (2) the two low energy features observed in the ELF cannot be explained by the surface phonon spectra [12,25] or in fact by a calculation of the ELF [25]. These peaks must result from $\vec{q}$-dependent EPC [7,38], which is indicated by the measured change in the phonon linewidth [14].

II. EXPERIMENT

The ARPES experiments were conducted at beamline 10.0.1 at the Advanced Light Source at the Lawrence Berkeley National Laboratory. The base pressure of the preparation chamber was in the low 10^{-10} torr range. The Be(0001) single-crystal surface was cleaned by cycles of sputtering at elevated temperature (450 °C) for 30 min followed by a 15-min annealing at 550 °C. In the sputtering procedure, Ar gas was used (8×10^{-6} torr) with a 1.5-keV beam energy. The sputtering beam was incident 45 deg off normal to the surface. When annealing, the pressure was at the range between the high 10^{-10} torr and low 10^{-9} torr range. ARPES measurements were performed in the main chamber with a base pressure in the low 10^{-11} torr range and were measured by a Scienta R4000 electron energy analyzer. The photon energy was set to be the first harmonic at 32 eV with a U10 undulator. Photon polarization is 90% out of sample plane while the angle between the incident photon and sample plane is ~7 deg. The orientation of the sample was determined by LEED and by the features in Fermi surface mapping. The sample was cooled by liquid helium to ~9 K during the measurements.

III. RESULTS: DETERMINATION OF THE ELF

Figure 3(a) shows the ARPES Fermi surface mapping on Be(0001), over approximately half of the surface Brillouin zone (BZ). Two surface states are seen at Fermi energy; the zone center $\bar{\Gamma}$ state and the zone boundary $\bar{M}$ state, consistent with previous reports [27]. It is known experimentally [23] and predicted theoretically [25] that the EPC is large around the Fermi contour of the $\bar{\Gamma}$ surface state. In the $\bar{\Gamma} \rightarrow \bar{M}$ direction the experimentally reported mass enhancement is 1.0 [23] while theory [25] predicts 1.17. High-quality energy-momentum dispersion maps along the $\bar{\Gamma} \rightarrow \bar{M}$ direction were recorded, as indicated by the red line in Fig. 3(a). Of the two surface states observed, we focus on the $\bar{\Gamma}$ state for the following discussions. The band dispersion in the $\bar{\Gamma} \rightarrow \bar{M}$ direction can be determined from the energy-momentum map by fitting the peak position of each momentum distribution curve (MDC) at each energy. Figure 3(b) shows a selected set of the MDCs from -0.2 to $+0.045$ eV. Figure 3(c) is the resulting energy dispersion obtained from the MDCs. A kink is observable near the binding energy ~60 meV, consistent with previous measurements [18–23].

Note that near the Fermi energy, a backward distortion in the dispersion [Fig. 3(c)] is present which originates from the convolution of the Fermi distribution edge and the energy resolution function. Guided by our simulations [39], the data with binding energy smaller than the energy resolution (13.4 meV) are discarded before performing further data analysis. One consequence of this procedure is that the Fermi momentum becomes an extra fitting parameter. In order to stabilize the fitting procedure, $\mathrm{Im}\Sigma(\varepsilon,\vec{k},T)$ is utilized as another constraint, which has not been done previously [9]. In addition to the $\mathrm{Re}\Sigma(\varepsilon,\vec{k},T)$ fitting, the minimization of the χ^2 to the $\mathrm{Im}\Sigma(\varepsilon,\vec{k},T)$ is also utilized in the analysis. $\mathrm{Im}\Sigma(\varepsilon,\vec{k},T)$ is obtained by converting the full width at half maximum (FWHM) of MDC $[\mathrm{Re}\Sigma(\varepsilon,\vec{k},T)]$ through the following relationship [40]:

$$\mathrm{Im}\Sigma(\varepsilon,\vec{k},T) = \frac{W_{\mathrm{MDC}}(\varepsilon,\vec{k},T)}{2} \cdot v(\varepsilon,\vec{k}), \tag{6}$$

where v is the effective bare-particle group velocity, defined as $v = \partial\varepsilon_0/\partial k$ ($\frac{\hbar^2}{m^*}k = 9.92 \times 10^{-39}k$ (kg$\frac{\mathrm{m}^3}{\mathrm{s}^2}$), SI units). Since

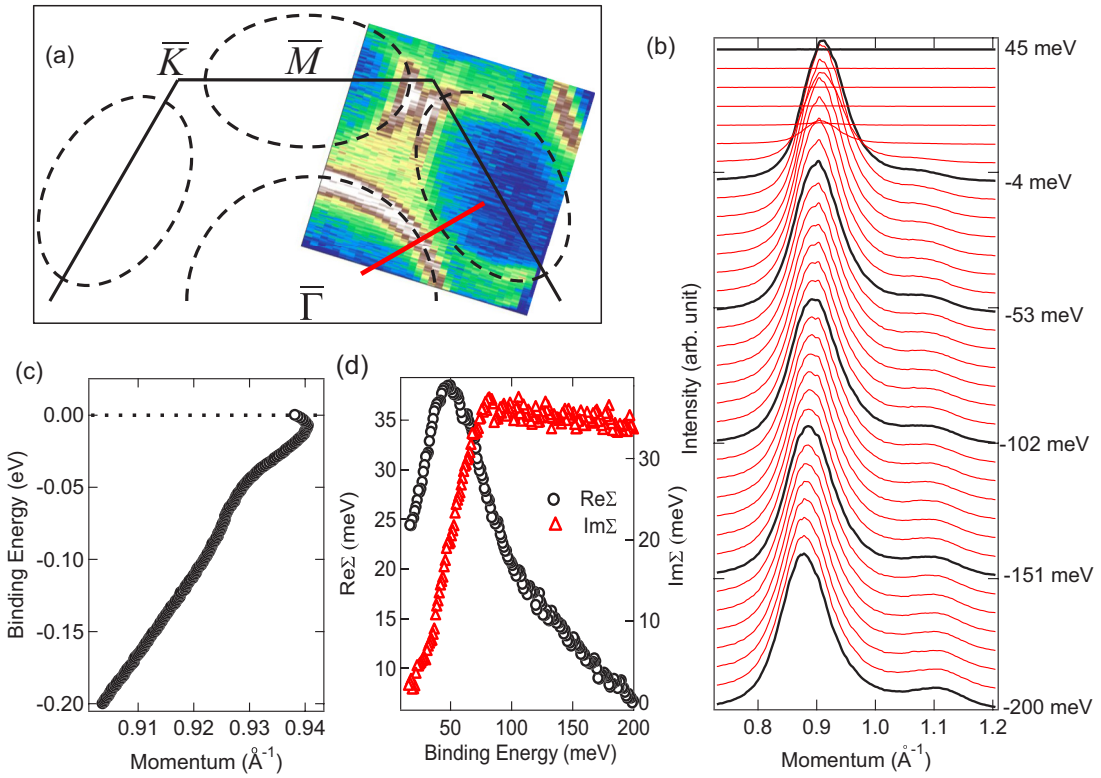

FIG. 3. (Color online) (a) Fermi surface mapping plotting with half of the Brillouin zone on Be(0001). Dashed circles/ellipses indicate the locations of $\bar{\Gamma}$ and $\bar{M}$ surface states. (b) Momentum distribution curves (MDC) of the energy-momentum mapping data along the $\bar{\Gamma} \rightarrow \bar{M}$ direction, indicated as the red line in (a). The MDCs are ranging from -0.2 to 0.045 eV with one plotted every seven spectra. For easy observation, every seven spectra in (b), the MDCs were labeled with its corresponding energy and were highlighted with bolded black solid lines while the rest are unbolded red solid lines. The prominent surface state disperses to the left when increasing binding energy corresponding to the $\bar{\Gamma}$ state. The weaker surface states disperse to the right corresponding to the $\bar{M}$ state. (c) Extracted electron dispersion relations from the MDC. (d) Extracted $\mathrm{Re}\Sigma(\varepsilon,\vec{k},T)$ and $\mathrm{Im}\Sigma(\varepsilon,\vec{k},T)$ from the electron dispersion relations shown in (c).

the fitted $\mathrm{Re}\Sigma(\varepsilon,\vec{k},T)$ and $\mathrm{Im}\Sigma(\varepsilon,\vec{k},T)$ are calculated from $\alpha^2F(\omega,\vec{k})$ through Eqs. (4) and (5), this procedure automatically fulfills the requirement of the Kramers-Kronig relationship between $\mathrm{Re}\Sigma(\varepsilon,\vec{k},T)$ and $\mathrm{Im}\Sigma(\varepsilon,\vec{k},T)$, and ensures the correctness of the choice of a bare-particle dispersion parameters, including the Fermi momentum parameter. It is worth noting that this procedure is equivalent to the method proposed to determine the bare-particle dispersion by using the self-consistent fitting between $\mathrm{Re}\Sigma(\varepsilon,\vec{k},T)$ and $\mathrm{Im}\Sigma(\varepsilon,\vec{k},T)$ [41]. The experimentally determined $\mathrm{Re}\Sigma(\varepsilon,\vec{k},T)$ and $\mathrm{Im}\Sigma(\varepsilon,\vec{k},T)$ are displayed in Fig. 3(d). It is standard procedure to subtract a constant term from the calculated $\mathrm{Im}\Sigma$ [39], which is done to produce the curve in Fig. 3(d).

Figure 4(a) shows again the self-consistently determined $\mathrm{Re}\Sigma(\varepsilon,\vec{k},T)$. Figure 4(b) is the extracted ELF $\alpha^2F(\omega,\vec{k})$ using MEM [9,37]. The basic idea of MEM is to perform the integral inversion with constraint of maximizing the entropy (see details in Refs. [9,37]). With our low noise data, there are several features revealed in the $\mathrm{Re}\Sigma(\varepsilon,\vec{k},T)$, which agree very well with the extracted $\alpha^2F(\omega,\vec{k})$ (vertical dashed lines). Remember, we removed the ARPES data with energy smaller than the instrumental energy resolution (13.4 meV) to avoid artifacts originating from the distorted raw data near Fermi energy. In the extracted $\alpha^2F(\omega,\vec{k})$, values of the function with energy smaller than 13.4 meV were constructed to be parabolic, $m_{\mathrm{cut}}(\omega/\omega_{\mathrm{cut}})^2$, and join on smoothly to $\alpha^2F(\omega,\vec{k})$ at the truncated energy ω_{cut} (in this case, 13.4 meV); where m_{cut} is a parameter for the fit in the modified MEM used here. The solid black line in Fig. 4(a) is the calculated $\mathrm{Re}\Sigma(\varepsilon,\vec{k},T)$ using the extracted ELF shown in Fig. 4(b). Ten peaks can be identified in the extracted $\alpha^2F(\omega,\vec{k})$. Their energies, contribution to ELF (in percentage), contribution to λ (value and percentage), and assignments (discussed later) are listed in Table I (will be discussed later).

Before discussing the origin of the peaks we need to describe the general representation of the mass enhancement factor λ introduced earlier, so that we can determine the relative contribution of surface vs bulk to λ. The mass enhancement factor is defined as first reciprocal moment of $\alpha^2F(\omega,\vec{k})$ [32]. Here we define a momentum-dependent, partial mass enhancement factor $\lambda'(\omega,\vec{k})$ as

$$\lambda'(\omega,\vec{k}) = 2\int_0^{\omega} \frac{\alpha^2F(\omega',\vec{k})}{\omega'}d\omega'. \tag{7}$$

The resulting $\lambda'(\omega,\vec{k})$ is shown in Fig. 4(c), where the total $\lambda = \lambda'(\infty,\vec{k}) = 0.94$. So once we have identified the origin of each peak in $\alpha^2F(\omega,\vec{k})$ we can calculate the contribution to λ. Hereafter we omit $\vec{k}$ notation in $\lambda'(\omega,\vec{k})$ for simplicity.

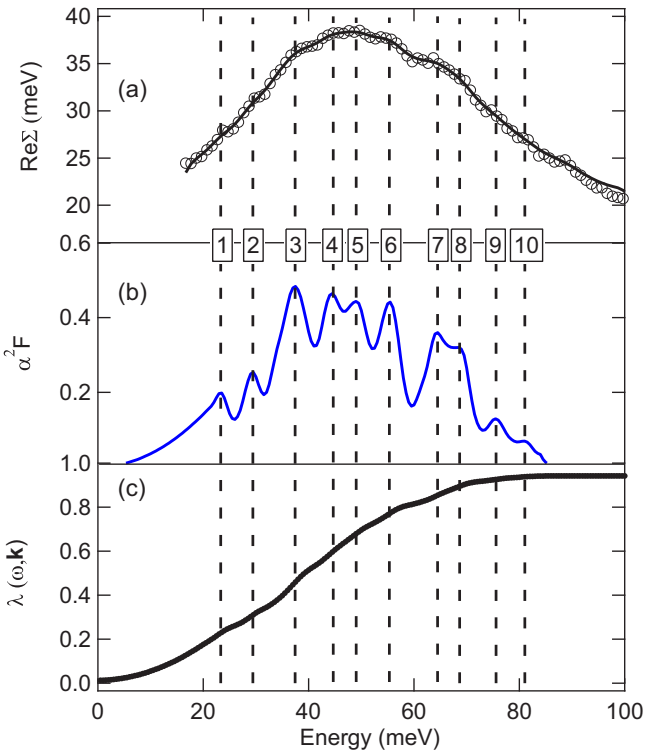

FIG. 4. (Color online) (a) The extracted $\mathrm{Re}\Sigma(\varepsilon,\vec{k},T)$ (black open circles), and fitted $\mathrm{Re}\Sigma(\varepsilon,\vec{k},T)$ (black solid line) as a function of binding energy. (b) The extracted $\alpha^2F(\omega,\vec{k})$. (c) The partial mass enhancement factors, $\lambda'(\omega,\vec{k})$ (see text for definition), calculated from the experimentally extracted $\alpha^2F(\omega,\vec{k})$.

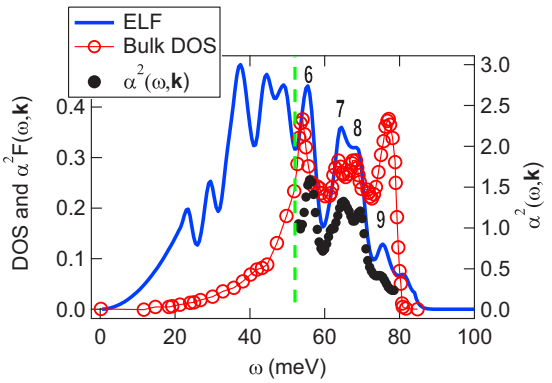

FIG. 5. (Color online) Comparison between the extracted ELF (blue solid line) and bulk phonon density of states (DOS) (red open circles) [40]. Peaks 6–9 in the ELF correspond to the peaks found in bulk phonon DOS, which is right to the green dashed line. The coupling constant $\alpha^2(\omega,\vec{k})$ (black solid circles) is obtained by dividing the ELF $\alpha^2F(\omega,\vec{k})$ by phonon DOS $F(\omega)$ in the bulk phonon energy range (50–80 meV).

IV. DISCUSSION

Let us start by comparing $\alpha^2F(\omega,\vec{k})$ to the bulk phonon DOS [42] in Fig. 5. It is obvious that peaks 6–9 are associated with the coupling of the surface states to the bulk phonons. The low energy tail of the bulk density of states overlaps the contribution from surface phonon modes, but for energies larger than ~52 meV (green vertical line) we can determine the energy dependence of the coupling constant $\alpha^2(\omega,\vec{k})$, which is shown in Fig. 5. Most likely $\alpha^2(\omega,\vec{k})$ is a smooth function, with the structure shown in Fig. 5 a result of the simplified picture that the ELF is proportional to the phonon DOS. To more accurately assign peaks in the extracted ELF to individual bulk phonon modes, we compare the extracted ELF to the bulk phonon dispersion curves in Fig. 6. In this figure the short horizontal red lines indicate the matches of peaks in ELF to flat regions in phonon dispersion curves. For example, peak 6 matches the flat region of the bulk phonon dispersion near Γ, and peak 4 aligns with the flat region near A in BZ. Using the comparison shown in Fig. 6, peaks 4–10 can be assigned to bulk phonon modes (Table I). The low bulk phonon DOS in Fig. 5 near the energy ranges for peaks 4 and 5 indicates that there should be other contributions other than bulk phonon modes responsible for the high ELF spectral weight. It will be discussed later that the other sources of the EPC for peaks 4 and 5 are from the surface phonon modes. Also note that peaks

TABLE I. Summarized ELF peak assignments along with the energy, the contribution to the ELF intensity in percentage, and the contribution to the mass enhancement factor (value and percentage). The peak numbers are defined in Fig. 4. The assignments are based on the comparison between the ELF and phonon DOS and dispersion relations (including bulk and surface phonon modes) (see Figs. 5–9).

Peak	ω (meV)	Contribution to ELF	Contribution to λ	Coupled phonon mode
1	22.3	11%	0.26(28%)	Surface RW Broadening
2	29.3	6%	0.08(8%)	Surface RW Broadening
3	37.5	19%	0.19(20%)	Surface RW Broadening Surface phonon at $\bar{M}$
4	44.5	13%	0.10(11%)	Surface phonon at $\bar{K}$ Bulk phonon near A
5	49.0	12%	0.09(10%)	Shear horizontal mode at $\bar{M}$ Bulk phonon near M
6	55.5	14%	0.09(10%)	Bulk phonon near Γ
7	64.5	13%	0.07(7%)	Bulk phonon near K and L
8	68.8	7%	0.03(3%)	Bulk phonon near M
9	75.5	4%	0.02(2%)	Bulk phonon near K
10	81.0	1%	0.01(1%)	Bulk phonon near Γ

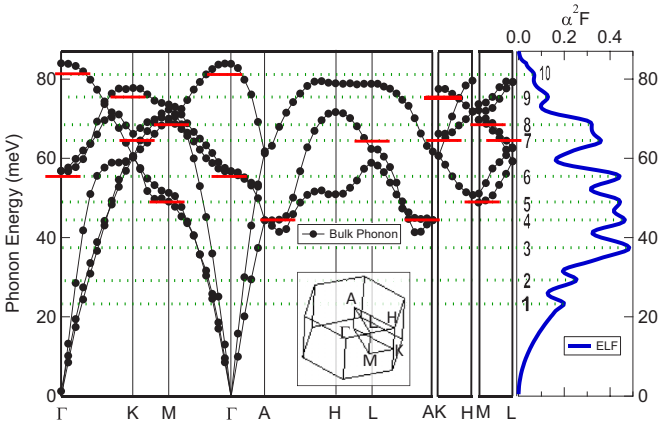

FIG. 6. (Color online) Summarized comparison between the extracted ELF and bulk phonon dispersion relations. Left panel shows the bulk phonon dispersions [42] (black solid circles). The right panel shows the extracted $\alpha^2F(\omega,\vec{k})$. Short red solid lines highlight the flat dispersion (high DOS) regions match to the peaks in the extracted $\alpha^2F(\omega,\vec{k})$. The high symmetric points in the momentum axis are indicated in the inset.

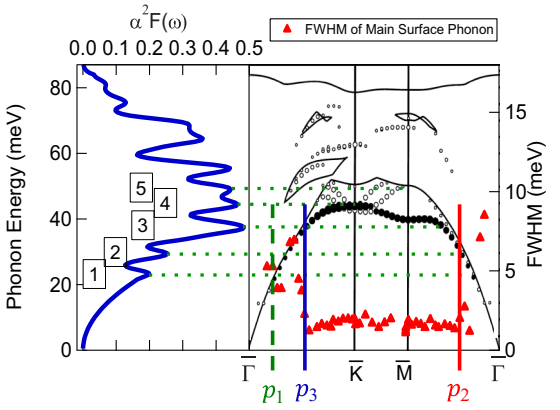

FIG. 7. (Color online) Comparison between extracted ELF (left panel) and calculated surface phonon dispersion. (Part of the right panel is adopted from Ref. [12]. Copyright 1998, the Elsevier.). Black solid (open) circles represent the modes localized more than 30% in the topmost layer (more than 50% in the three topmost layers) [12]. Red triangles show the width of the strong peaks [13]. The projected bulk phonon modes are represented by the area enclosed by black solid lines. Two vertical solid lines indicate the momenta [$\vec{p}_2$ in $\bar{\Gamma} \rightarrow \bar{M}$ (red) and $\vec{p}_3$ in $\bar{\Gamma} \rightarrow \bar{K}$ (blue)] where the surface RW linewidth has a dramatic increase. $\vec{p}_2$ and $\vec{p}_3$ also match to the momenta where peaks 2 and 3 intersect with the surface RW dispersion relationship, respectively. One vertical green dashed line indicates the momentum ($\vec{p}_1$ in $\bar{\Gamma} \rightarrow \bar{K}$ direction) where another surface RW linewidth change near zone center. $\vec{p}_1$ matches where peak 1 intersects with the surface RW dispersion relationship.

9 and 10 do not match exactly with features in phonon DOS (see Fig. 5), but this small discrepancy could easily originate from ω or $\vec{k}$ dependence of $\alpha^2(\omega,\vec{k})$, or to restrictions in the final state $\vec{k}'$ that we have not yet discussed.

The contribution of the surface phonon modes to the ELF can be determined by comparing $\alpha^2F(\omega,\vec{k})$ to the calculated surface phonon dispersion by Lazzeri and de Gironcoli [12] and measured dispersion by Hannon *et al.* [13]. In the right panel of Fig. 7, the solid (open) dots indicated the calculated modes with large (small) surface amplitude [12]. The solid triangles at the bottom indicate the measured FWHM of the RW using high-resolution electron energy loss spectroscopy (HREELS) [13]. It is clear that peak 4 can be associated with high density of states in the surface RW (flat region) at $\bar{K}$; while peak 5 could be associated with the shear horizontal mode at $\bar{M}$ [13,43]. Experimentally the energy of the shear horizontal mode was determined to be ∼50.5 meV, which is very close to energy of peak 5 (49.0 meV). Therefore, peaks 4 and 5 could involve contributions from both surface and bulk phonon modes (Fig. 6). Peak 3 does not line up exactly with a flat part of the dispersion of the RW from $\bar{\Gamma} \rightarrow \bar{M}$, but again this could be a consequence of the matrix element, shape of phonon dispersion away from the high symmetry direction, or restrictions in available final states $\vec{k}'$. Based on these comparisons, the assignments obtained from the comparisons presented in Figs. 6 and 7 the assignments for peaks 3–10 are given in Table I. What could be concluded here is that there is a range of energy (41–52 meV) where the contributions to the ELF gradually transit from the surface RW modes (31.5–52 meV) to the bulk modes (41–80 meV).

The assignments of peaks 1 and 2 are still outstanding, however they should be associated with the RW at the surface since Fig. 6 shows there is nothing in the bulk phonon spectra in this energy range. Importantly, the data of Hannon *et al.* showed that there was a dramatic change in the RW linewidth in this low energy (small momentum) region, as shown by the red triangles in Fig. 7 [13]. Interestingly, the momenta where these width changes occur appear to coincide with the low lying peaks in the ELF, peak 1 with $\vec{p}_1$, peak 2 with $\vec{p}_2$, and peak 3 with $\vec{p}_3$. In particular, $\vec{p}_2$ and $\vec{p}_3$ coincide with the momenta where the surface RW linewidth suddenly increases along $\bar{\Gamma}$-$\bar{M}$ and $\bar{\Gamma}$-$\bar{K}$ directions, respectively. These authors speculated that surface Rayleigh mode dispersion entered into the region of bulk projected phonon bands, causing the abrupt change in phonon linewidth, but this behavior is not seen in calculated surface phonon dispersion by Lazzeri and de Gironcoli [12]. In principle, this strange behavior could result from Fermi surface nesting, but we will demonstrate that this is not the case and moreover the behavior was not reproduced with sophisticated phonon calculation [12]. Most likely peaks 1–3 result from a $\vec{q}$-dependent EPC matrix element as seen in the layered transition metal dichalcogenides and cuprates, not from any form of Fermi surface nesting [7,38]. The $\vec{q}$-dependent EPC manifests itself in changes in the phonon width and energy as a function of $\vec{q}$ [7,38] and would not be reproduced in a phonon dispersion calculation.

The final and most important step is to use our data and analysis to determine the location of the final electron state $\vec{k}'$ for the assigned $\vec{q}$ of the phonon modes (Figs. 6 and 7). This progress requires both energy and momentum conservation, but considering the phonon energy, in the range of 0–80 meV, the constant energy contour of the final states is only ∼1.5% smaller than the Fermi contour. In other words, the initial states and final states contours are not distinguishable in the scale used in Fig. 1(b), so we will assume $\varepsilon(\vec{k}') - \varepsilon(\vec{k}) = 0$.

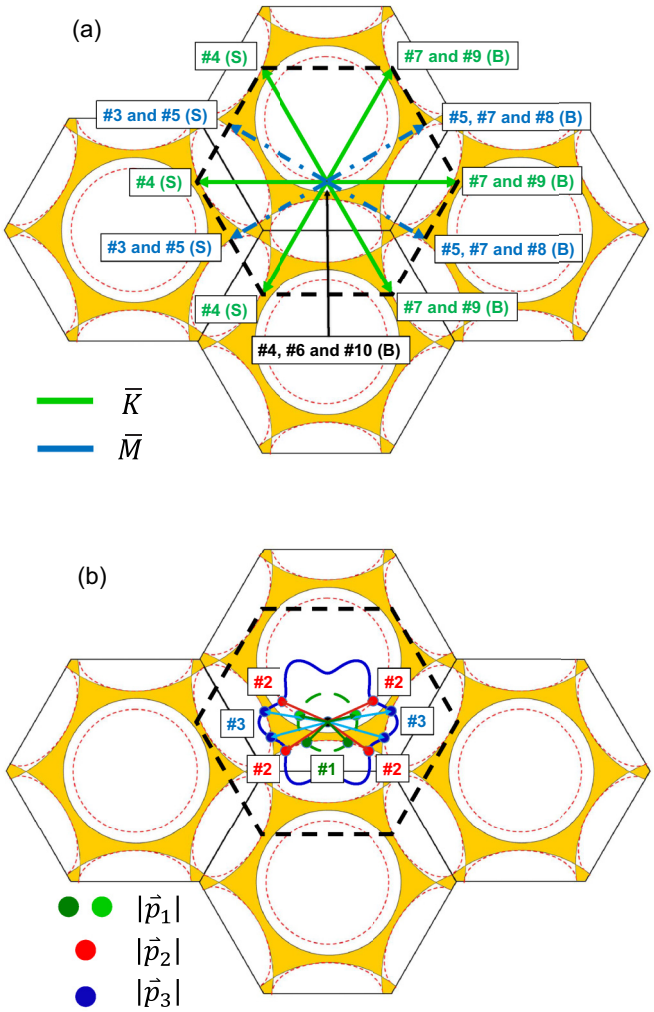

FIG. 8. (Color online) (a) Starting at $\bar{\Gamma}$ state along the $\bar{\Gamma} \rightarrow \bar{M}$ direction as the initial state $\vec{k}$ mediating by phonon modes with momenta as $M(\bar{M})$ (blue dashed arrows) and $K(\bar{K})$ (green solid arrows). Peaks 3–10 are assigned and labeled: bulk modes are labeled to the right; while the surface modes are labeled to the left, for easy reading. (b) Starting at $\bar{\Gamma}$ state along the $\bar{\Gamma} \rightarrow \bar{M}$ direction as the initial state $\vec{k}$ mediating by phonon modes with momenta $\vec{p}_1$ (green arrows and green arc segments), or with a momentum contour where the surface RW linewidth has sudden changes (blue solid contour). The final states corresponding to ELF peaks 1, 2, and 3 are represented by green, red, and blue dots, respectively. The definitions of $\vec{p}_1$ through $\vec{p}_3$ could be found in Fig. 7. Extended BZs are plotted with black solid hexagons, while surface states are indicated as red dashed circles and ellipses. Black dashed hexagon is the same as BZ, centered at initial state where the ARPES measured, and is used to assist view of the phonon momenta.

Our measurements were conducted on $\bar{\Gamma}$ state along $\bar{\Gamma}$-$\bar{M}$ direction, so we know $\vec{k}$, as indicated as the starting point in Fig. 8.

The search for the final states $\vec{k}'$ requires momentum conservation from the initial state on the $\bar{\Gamma}$ surface state to possible electronic states either bulk (shaded regions) or surface (dashed lines) in Fig. 8. The surface is a source of momentum perpendicular to the surface [44], so all that needs to be considered for a bulk electron or phonon state is the momentum projected onto the surface BZ, namely $\vec{q}_{\parallel} = \vec{k}' - \vec{k}$. First consider peaks 6 and 10 as a simple example of bulk phonon modes. Figure 6 shows that both of these peaks are associated with phonons in the bulk near zone center momentum Γ. The momentum component parallel to the surface is zero so $\vec{k}' = \vec{k}$, as labeled in Fig. 8(a). Next look at peak 4, which according to Fig. 6 could be associated with flat phonon dispersion near A along A-H and A-L direction in the bulk, or according to Fig. 7 the region in the RW surface phonon mode near $\bar{K}$. For the 2D BZ, A is projected onto $\bar{\Gamma}$ in the surface BZ, so if peak 4 is bulk then $\vec{k}' = \vec{k}$. If peak 4 is from the RW surface phonon band $\vec{q} = \bar{\mathrm{K}}$. Both options are shown in Fig. 8(a), where for the surface excitation the transition is from the $\bar{\Gamma}$ surface state to the $\bar{M}$ surface state (mediated by surface phonon mode near $\bar{K}$). A final example is bulk peak 9 associated with a high phonon DOS at K in the bulk, which corresponds to the $\bar{K}$ in the surface. Figure 8(a) shows that this is again an electronic transition from the $\bar{\Gamma}$ surface state to the $\bar{M}$ surface state. Following the procedure outlined in these examples all the higher energy peaks (3–10) for both surface and bulk phonon modes have been labeled in Fig. 8(a). Surprisingly, many of the electronic transitions are from the $\bar{\Gamma}$ surface state to the $\bar{M}$ surface state.

Finally, let us discuss the low energy peaks $1 \rightarrow 3$. As stated previously, there is a remarkable connection between the energies of these peaks in the ELF and the measured linewidth changes in the RW surface phonon mode [13]. The abrupt increase in the RW linewidth at $\vec{p}_3$ in the $\bar{\Gamma} \rightarrow \bar{K}$ direction must be associated with $\vec{p}_2$ in the $\bar{\Gamma} \rightarrow \bar{M}$, so a contour in k space for this behavior should be continuous, which we have attempted to draw in Fig. 8(b). In contrast, there is no sign of the linewidth change at $\vec{p}_1$ in the $\bar{\Gamma} \rightarrow \bar{M}$ direction, so we plot only segments in $\bar{\Gamma} \rightarrow \bar{K}$ directions.

First consider peak 1, which according to Fig. 7 could be associated $\vec{p}_1$ or $\vec{p}_3$ in the $\bar{\Gamma} \rightarrow \bar{K}$ direction or $\vec{p}_2$ in the $\bar{\Gamma} \rightarrow \bar{M}$ direction. Figure 8(b) (green dots) shows that the only possible transitions for peak 1 are associated $\vec{p}_1$ slightly off of the $\bar{\Gamma} \rightarrow \bar{K}$ direction. Most likely peak 1 is associated with a transition from $\bar{\Gamma}$ surface state to the $\bar{M}$ surface state (dark green dots). Peak 2, as shown in Fig. 8(b), could be a transition from the $\bar{\Gamma}$ surface state to either the $\bar{\Gamma}$ or $\bar{M}$ surface states (red dots). Peak 3, which as indicated in Fig. 7, could be associated with the linewidth broadening of the RW with momentum $\vec{p}_3$ in the $\bar{\Gamma} \rightarrow \bar{K}$ direction. Figure 8(b) shows that there are no final states for such a transition. However, there is a possibility that peak 3 is associated with a transition from $\bar{\Gamma}$ surface state to the $\bar{M}$ surface state as shown in Fig. 8(b) (blue dots), slightly off the $\bar{\Gamma} \rightarrow \bar{K}$ direction. Thus, peak 3 is assigned to both the RW linewidth broadening and the surface RW mode at $\bar{M}$ [Fig. 8(a)]. It should be pointed out that there is no possibility of EPC resulting from Fermi surface nesting [Fig. 8(b)] consistent with recent work showing that Fermi surface nesting is not relevant to charge density wave formation in quasi-two-dimensional materials [38].

The different contributions to the ELF function and mass enhancement factors for the ten modes are summarized in Table I. These numbers are the values of $\alpha^2 F(\omega, \vec{k}; i)$

and $\lambda'(\omega,\vec{k};i)$ for $i = 1$ to 10. The conclusion is that $\sim 51.5 \pm 12.5\%$ of the ELF intensity and $\sim 33.5 \pm 10.5\%$ of the mass enhancement come from bulk phonon mediated processes (peaks 6–10 and part of 4 and 5). Given that the total mass enhancement is 0.94, the bulk contributes $\sim 0.31 \pm 0.10$, which is accidentally similar to the bulk value (0.24) [45]. In other words, the rest of the contribution ($\sim 48.5 \pm 12.5\%$ of the ELF intensity and $\sim 66.5 \pm 10.5\%$ of the mass enhancement) comes from the presence of surface phonon modes, including the contribution from the surface RW phonon linewidth broadening related coupling. On the other hand, the contributions solely from the RW modes (part of 3, 4, and 5) are $\sim 44 \pm 22\%$ of the ELF and $\sim 41 \pm 20.5\%$ of mass enhancement. The RW broadening related coupling (1, 2, and part of 3) contributes $\sim 26.5 \pm 9.5\%$ of the ELF and $\sim 46 \pm 10\%$ of the mass enhancement. These numbers are a little misleading since Fig. 8 shows that the initial and final electron states are most frequently on surface states. If there were no surface states the results would be fundamentally different.

It is important to remember that the observed behavior of the dispersion and linewidth of the RW has not been explained theoretically, even with the best calculations of the surface phonon dispersion [12]. This is not surprising if the dramatic increase in the width is caused by a $\vec{q}$-dependent EPC matrix element. What is surprising is the fact that a sophisticated calculation of the ELF for Be(0001) [25] does not produce any peaks in this low energy range. In fact, none of the features in our data are reproduced by this calculation! Figure 9 compares the experimental and the calculated [25] $\alpha^2F(\omega,\vec{k})$ and $\mathrm{Re}\Sigma(\varepsilon,\vec{k},T)$ at Fermi energy along the $\bar{\Gamma} \rightarrow \bar{M}$ direction. The mass enhancements are similar, 1.17 from theory and 0.94 from experiment, but nothing else agrees. The conspicuous difference in ELF is the huge contribution in the theory at 41 meV from the RW at an energy where the experimental data has a valley. Experimental peaks 4, 5, and 7 all occur at energies where there are valleys in the theoretical ELF. Only peaks 6 and 9 seem to agree with theory. By using Eq. (4), $\mathrm{Re}\Sigma(\varepsilon,\vec{k},T)$ is calculated from the theory and compared with experiment [same Fig. 4(a)] in Fig. 9(b). The large peak at 41 meV in the theoretical ELF results in a strong peak in $\mathrm{Re}\Sigma(\varepsilon,\vec{k},T)$ and makes the theoretical $\mathrm{Re}\Sigma(\varepsilon,\vec{k},T)$ as large ($\sim$80 meV) as twice of the experimental counterpart ($\sim$40 meV) at 50 meV binding energy. Note that all the reported experimental $\mathrm{Re}\Sigma(\varepsilon,\vec{k},T)$ for Be(0001) $\bar{\Gamma}$ surface state are in the range of 40–50 meV at 50 meV binding energy [19,21–23], which further questions the theoretical ELF [25]. As discussed in Fig. 2, missing low energy peaks in the ELF and with similar λ in the theoretical calculation will result in larger $\mathrm{Re}\Sigma(\varepsilon,\vec{k},T)$, compared to the experimental counterparts. In principle, this calculation should have captured the features associated with the $\vec{q}$-dependent EPC matrix element. The dramatic difference between theory and experiment shown in Fig. 9 illustrates our original argument, that it is much harder to understand EPC in an environment of broken symmetry than in a 2D system.

One of the most interesting phenomena discovered here was the enhancement in the EPC associated with the surface RW broadening. This interaction is a result of the broken symmetry, rather than merely the low dimensionality of the surface states and surface phonon modes. The existence of the surface phonon modes as well as the electronic surface states are the results of the translational broken symmetry on the surfaces. The difference between Eqs. (1) and (3) is not just the level of complication, but rather the effect on of broken symmetry on EPC matrix element.

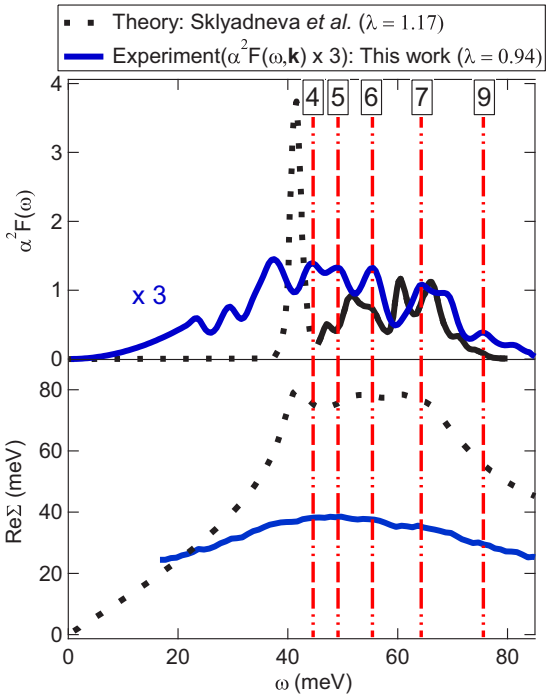

FIG. 9. (Color online) Top panel: Comparison between the experimental and theoretical $\alpha^2F(\omega,\vec{k})$ along the $\bar{\Gamma} \rightarrow \bar{M}$ direction [25] at $\bar{\Gamma}$ state. The dashed portion of the black line represents the contributions from surface RW [25]; while the experimental curve is the experimental ELF multiplied with a factor of 3 for easy comparison. Bottom panel: Comparison between the experimental and theoretical $\mathrm{Re}\Sigma(\varepsilon,\vec{k},T)$ along the $\bar{\Gamma} \rightarrow \bar{M}$ direction at $\bar{\Gamma}$ state. The theoretical $\mathrm{Re}\Sigma(\varepsilon,\vec{k},T)$ is calculated from the theoretical ELF in the top panel from Eq. (4).

V. CONCLUSION

In conclusion, the comparison between the structure in the extracted $\alpha^2F(\omega,\vec{k})$ and phonon dispersions and/or phonon DOS has allowed us to determine in detail the origin of different contributions to the mass enhancement. The enhanced EPC on the Be(0001) surface compared to the bulk counterpart is mainly due to the presence of surface RW, including peaks in the ELF related to the RW broadening, which is not captured by theoretical calculations. The broken symmetry is argued to be responsible for the strong enhancement of the electron-phonon coupling for the case of the Be(0001). The analysis shown here requires information of the bulk and surface phonon DOS, phonon dispersion relationships, and the electronic band structure near Fermi energy to identify the final states.

ACKNOWLEDGMENTS

This work was supported by the National Science Foundation, TYC by DMR-0451163; and EWP by DMR-1504226. The ALS is supported by the Office of Basic Energy Sciences, of the U.S. Department of Energy under Contract No. DE-AC02-05CH11231.

[1] O. Gunnarsson and O. Rösch, J. Phys. Condens. Matter **20**, 043201 (2008).
[2] M. L. Kulic, Phys. Rep. **338**, 1 (2000).
[3] J. P. Carbotte, Rev. Mod. Phys. **62**, 1027 (1990).
[4] A. Majumdar and P. Reddy, Appl. Phys. Lett. **84**, 4768 (2004).
[5] J. Hodak, I. Martini, and G. V. Hartland, Chem. Phys. Lett. **284**, 135 (1998).
[6] A. J. Millis, B. I. Shraiman, and R. Mueller, Phys. Rev. Lett. **77**, 175 (1996).
[7] M. D. Johannes and I. I. Mazin, Phys. Rev. B **77**, 165135 (2008).
[8] B. C. Hsu, Y.-S. Liu, S. H. Lin, and Y.-C. Chen, Phys. Rev. B **83**, 041404(R) (2011).
[9] J. Shi, S.-J. Tang, B. Wu, P. T. Sprunger, W. L. Yang, V. Brouet, X. J. Zhou, Z. Hussain, Z.-X. Shen, Z. Zhang, and E. W. Plummer, Phys. Rev. Lett. **92**, 186401 (2004).
[10] L. Zhao, J. Wang, J. Shi, W. Zhang, H. Liu, J. Meng, G. Liu, X. Dong, J. Zhang, W. Lu, G. Wang, Y. Zhu, X. Wang, Q. Peng, Z. Wang, S. Zhang, F. Yang, C. Chen, Z. Xu, and X. J. Zhou, Phys. Rev. B **83**, 184515 (2011).
[11] E. V. Chulkov, V. M. Silkin, and E. N. Shirykalov, Surf. Sci. **188**, 287 (1987).
[12] M. Lazzeri and S. De Gironcoli, Surf. Sci. **402–404**, 715 (1998).
[13] J. B. Hannon, E. J. Mele, and E. W. Plummer, Phys. Rev. B **53**, 2090 (1996).
[14] M. Mostoller, R. M. Nicklow, D. M. Zehner, S.-C. Lui, J. M. Mundenar, and E. W. Plummer, Phys. Rev. B **40**, 2856 (1989).
[15] B. Diaconescu, K. Pohl, L. Vattuone, L. Savio, P. Hofmann, V. M. Silkin, J. M. Pitarke, E. V Chulkov, P. M. Echenique, D. Farías, and M. Rocca, Nature (London) **448**, 57 (2007).
[16] H. Qin, J. Shi, Y. Cao, K. Wu, J. Zhang, E. W. Plummer, J. Wen, Z. J. Xu, G. D. Gu, and J. Guo, Phys. Rev. Lett. **105**, 256402 (2010).
[17] G. D. Mahan and E. W. Plummer, in *Electronic Structure*, edited by K. Horn and M. Scheffler, Handbook of Surface Science, Vol. 2 (Elsevier, Amsterdam, 2000), Chap. 14, pp. 953–987.
[18] T. Balasubramanian, E. Jensen, X. L. Wu, and S. L. Hulbert, Phys. Rev. B **57**, R6866 (1998).
[19] M. Hengsberger, R. Frésard, D. Purdie, P. Segovia, and Y. Baer, Phys. Rev. B **60**, 10796 (1999).
[20] M. Hengsberger, D. Purdie, P. Segovia, M. Garnier, and Y. Baer, Phys. Rev. Lett. **83**, 592 (1999).
[21] S. LaShell, E. Jensen, and T. Balasubramanian, Phys. Rev. B **61**, 2371 (2000).
[22] S.-J. Tang, J. Shi, B. Wu, P. T. Sprunger, W. L. Yang, V. Brouet, X. J. Zhou, Z. Hussain, Z.-X. Shen, Z. Zhang, and E. W. Plummer, Phys. Status Solidi **241**, 2345 (2004).
[23] T.-Y. Chien, E. D. L. Rienks, M. F. Jensen, P. Hofmann, and E. W. Plummer, Phys. Rev. B **80**, 241416(R) (2009).
[24] A. Eiguren, S. de Gironcoli, E. V. Chulkov, P. M. Echenique, and E. Tosatti, Phys. Rev. Lett. **91**, 166803 (2003).
[25] I. Y. Sklyadneva, E. V. Chulkov, P. M. Echenique, and A. Eiguren, Surf. Sci. **600**, 3792 (2006).
[26] U. O. Karlsson, S. A. Flodström, R. Engelhardt, W. Gädeke, and E. E. Koch, Solid State Commun. **49**, 711 (1984).
[27] R. A. Bartynski, E. Jensen, T. Gustafsson, and E. W. Plummer, Phys. Rev. B **32**, 1921 (1985).
[28] P. J. Feibelman and R. Stumpf, Phys. Rev. B **50**, 17480 (1994).
[29] H. J. Choi, D. Roundy, H. Sun, M. L. Cohen, and S. G. Louie, Nature (London) **418**, 758 (2002).
[30] M. Lazzeri, C. Attaccalite, L. Wirtz, and F. Mauri, Phys. Rev. B **78**, 081406(R) (2008).
[31] J. L. McChesney, A. Bostwick, T. Ohta, T. Seyller, K. Horn, J. González, and E. Rotenberg, Phys. Rev. Lett. **104**, 136803 (2010).
[32] G. Grimvall, *The Electron-Phonon Interactions in Metals* (Elsevier, New York, 1981).
[33] T. Valla, A. V. Fedorov, P. D. Johnson, B. O. Wells, S. L. Hulbert, Q. Li, G. D. Gu, and N. Koshizuka, Science **285**, 2110 (1999).
[34] X. J. Zhou, J. Shi, T. Yoshida, T. Cuk, W. L. Yang, V. Brouet, J. Nakamura, N. Mannella, S. Komiya, Y. Ando, F. Zhou, W. X. Ti, J. W. Xiong, Z. X. Zhao, T. Sasagawa, T. Kakeshita, H. Eisaki, S. Uchida, A. Fujimori, Z. Zhang, E. W. Plummer, R. B. Laughlin, Z. Hussain, and Z. X. Shen, Phys. Rev. Lett. **95**, 117001 (2005).
[35] W. Zhang, G. Liu, L. Zhao, H. Liu, J. Meng, X. Dong, W. Lu, J. S. Wen, Z. J. Xu, G. D. Gu, T. Sasagawa, G. Wang, Y. Zhu, H. Zhang, Y. Zhou, X. Wang, Z. Zhao, C. Chen, Z. Xu, and X. J. Zhou, Phys. Rev. Lett. **100**, 107002 (2008).
[36] W. Meevasana, N. J. C. Ingle, D. H. Lu, J. R. Shi, F. Baumberger, K. M. Shen, W. S. Lee, T. Cuk, H. Eisaki, T. P. Devereaux, N. Nagaosa, J. Zaanen, and Z. X. Shen, Phys. Rev. Lett. **96**, 157003 (2006).
[37] J. E. Gubernatis, M. Jarrell, R. N. Silver, and D. S. Sivia, Phys. Rev. B **44**, 6011 (1991).
[38] X. Zhu, Y. Cao, J. Zhang, E. W. Plummer, and J. Guo, Proc. Natl. Acad. Sci. USA **112**, 2367 (2015).
[39] See Supplemental Material at http://link.aps.org/supplemental/10.1103/PhysRevB.92.075133 for the distortion of dispersion curve near Fermi energy.
[40] A. Kaminski, M. Randeria, J. C. Campuzano, M. R. Norman, H. Fretwell, J. Mesot, T. Sato, T. Takahashi, and K. Kadowaki, Phys. Rev. Lett. **86**, 1070 (2001).
[41] A. A. Kordyuk, S. V. Borisenko, A. Koitzsch, J. Fink, M. Knupfer, and H. Berger, Phys. Rev. B **71**, 214513 (2005).
[42] R. Stedman, Z. Amilius, R. Pauli, and O. Sundin, J. Phys. F Met. Phys. **6**, 157 (1976).
[43] J. B. Hannon and E. W. Plummer, J. Electron Spectrosc. Relat. Phenom. **64-65**, 683 (1993).
[44] A. Damascelli, Phys. Scr. **T109**, 61 (2004).
[45] G. D. Mahan, *Many-Particle Physics, Physics of Solids and Liquids* (Kluwer Academic/Plenum, New York, 2000).